


RESEARCH ARTICLE

Structural health monitoring of 52-meter wind turbine blade: Detection of damage propagation during fatigue testing

Mads A. Fremmelev^{1,4,*} , Purim Ladpli¹, Esben Orlowitz², Lars O. Bernhammer³, Malcolm McGugan⁴ and Kim Branner⁴

¹Siemens Gamesa Renewable Energy, Offshore Blade Technology Department, Assensvej 11, 9220 Aalborg East, Denmark

²Siemens Gamesa Renewable Energy, Turbine Monitoring and Operation Department, Borupvej 16, 7330 Brande, Denmark

³Siemens Gamesa Renewable Energy, Onshore Blade Technology Department, Avenida Ciudad de la Innovación, 2, 31621 Sarriguren, Navarra, Spain

⁴Technical University of Denmark, Department of Wind Energy, Frederiksborgvej 399, 4000 Roskilde, Denmark

*Corresponding author. E-mail: mads.fremmelev@siemensgamesa.com

Received: 27 November 2021; **Revised:** 07 March 2022; **Accepted:** 29 March 2022

Keywords: Damage; fatigue testing; structural health monitoring; wind turbine blades

Abstract

This work is concerned with damage detection in a commercial 52-meter wind turbine blade during fatigue testing. Different artificial damages are introduced in the blade in the form of laminate cracks. The lengths of the damages are increased manually, and they all eventually propagate and develop into delaminations during fatigue loading. Strain gauges, acoustic emission sensors, distributed accelerometers, and an active vibration monitoring system are used to track different physical responses in healthy and damaged states of the blade. Based on the recorded data, opportunities and limitations of the different sensing systems for blade structural health monitoring are investigated.

Impact Statement

Blades are among the costliest components of a wind turbine, both in terms of manufacturing as well as maintenance. To reduce the cost of wind turbines, and thus reduce the levelized cost of wind energy, monitoring the health of blades during operation is necessary. This may be done through structural health monitoring (SHM), where sensors are used to monitor the structural response of blades during operation. This work contributes to the topic of blade SHM by studying how the structural response of a blade is affected by damages. Different sensing systems are installed on the blade, and their capabilities as well as limitations for detection of damage are investigated.

1. Introduction

With increasing investments in wind energy being made, there is an increasing desire for ensuring turbine uptime and longevity from developers, owners, and original equipment manufacturers. Blades are among the most critical and expensive components in wind turbines, both in terms of manufacturing and repair cost (Dao et al., 2019). Over the life of an operating turbine, preexisting manufacturing defects in blades may develop into critical damages, which may eventually result in blade failure. Thus, surveillance of blade performance in operating turbines is becoming increasingly desirable. One way to achieve this is through the use of structural health monitoring (SHM) systems. Using sensors, the physical response of

blades is measured, and signal processing algorithms are used to determine if there are any significant changes to the blade performance. Design and test of SHM systems for wind turbine blades has been a topic of interest for researchers for several decades. An inhibiting factor for the progress of this topic of research is the limited number of full-scale tests performed with progressive damages in blades, both for operating wind turbines and wind turbine blade tests.

Table 1 lists literature on the topic of wind turbine blade SHM in laboratory environments, during fatigue testing, and for an operating turbine. The table also includes an overview of sensing systems used and damage types. Different types of sensing systems have been investigated for use in SHM of wind turbine blades, including strain sensors, deflection sensors, digital image correlation (DIC), accelerometers, acoustic emission (AE), and guided waves (GW).

Strain gauges (SGs), measuring strain locally at single points, are commonly used during blade testing to monitor the applied load level. Since this type of sensor is already present, a secondary use for damage detection would add to the usefulness of the sensor. SGs were shown to indicate damage propagation through nonlinear load–strain behavior by, for example, Sundaresan et al. (2002) and Jørgensen et al. (2004), as well as Overgaard et al. (2010) and Overgaard and Lund (2010) under quasi-static loading. Under fatigue loading, Paquette et al. (2008) and Rumsey et al. (2008) used SG data to capture stiffness degradation over time, indicating fatigue aging of the blade. Chen (2019) and Chen et al. (2021) used decay of the strain amplitude over time to indicate fatigue-driven damage propagation. The performance of conventional electrical resistance foil gauges, fiber Bragg gratings (FBGs), and distributed optical strain sensors was compared by Sierra-Pérez et al. (2016) for damage detection during quasi-static testing. The conventional SGs and FBGs, which both measure pointwise strain, showed similar performance in measurement accuracy and capabilities for damage detection. However, the authors pointed out practical advantages of FBGs, such as embedding during manufacture, longer lifetime, and electromagnetic immunity. Use of distributed optical sensors also provided some advantages, mainly being the ability to measure strain at multiple points.

Deflection of blades, both global and local, has been studied in literature. Global deflection shapes are commonly used to validate blade finite element (FE) models, and local deflections are used as an indicator for the development of damage. Propagation of damage under quasi-static loading was captured through nonlinear local load–displacement behavior of the spar cap by Sørensen et al. (2004) as well as by Overgaard et al. (2010) and Overgaard and Lund (2010). Haselbach et al. (2016) as well as Haselbach and Branner (2016) used draw wire displacement transducers and stereophotogrammetry to capture nonlinear trailing edge (TE) displacements caused by local buckling.

DIC is another sensing system, which has received interest from researchers for use in damage detection in wind turbine blades. Using a random black-and-white speckle pattern applied to an area of the blade, displacements can be inferred, and strains can be calculated based on theory of elasticity principles. An advantage over, for example, SGs is that raw displacement data are available, and that strains can be calculated for a larger area with a good spatial resolution. There are both 2D and 3D DIC systems available, which use a single and two cameras, respectively. 2D systems can capture in-plane displacements, whereas 3D systems can also capture out-of-plane displacements. Chen et al. (2019) investigated failure of a wind turbine blade TE section subjected to quasi-static loading. A 3D DIC system was used to measure out-of-plane deformations and to capture buckling-driven failure of the component. A 3D DIC system was used by LeBlanc et al. (2011) to monitor critical areas of a blade during quasi-static testing. Increases in strain amplitude as well as discontinuities in calculated curvatures were used to locate two different damages in the blade and to monitor the progression of the damages. Poozesh et al. (2017) used a 3D DIC system during fatigue testing, and time histories of flapwise deflection as well as in-plane normal strains were recorded successfully. The 3D DIC system consisted of two cameras, placed on the ground and recording the external suction side (SS) root area, which recorded 215 images over a 30-s period of fatigue testing. By use of the recorded images, the cyclic variation in strain distribution in the recorded area could be investigated during fatigue testing. A method for using multiple DIC systems to survey the surface of an entire blade was proposed and validated on a reduced-scale blade. The proposed method was also useful for performing operational modal analysis (OMA) on a blade. Chen et al. (2021)

Table 1. Literature on structural health monitoring (SHM) of full-scale wind turbine blades.

Authors	Loading	Sensing systems	Coverage	Damage types	Detection	Blade length (m)
Larsen et al. (2014)	S-S	ACC	GLOB	DEBOND	IN, PROP, LOC	34.0
Tcherniak and Mølgaard (2015)						
Sundaresan et al. (2002)	QS	GW, SG	POINT, LOC	BUCK	PROP	9.0
Jørgensen et al. (2004)	QS	AE, LVDT, SG	POINT, LOC	DEL, FF	IN	25.0
Sørensen et al. (2004) and Jensen et al. (2006)	QS	LVDT, SG	POINT	BUCK, DEL	PROP, LOC	34.0
Overgaard et al. (2010)	QS	AE, LVDT, SG	POINT, LOC	BUCK, DEL	IN, PROP, LOC	25.0
LeBlanc et al. (2011)	QS	DIC	LOC	Crack	IN, PROP, LOC	9.0
Yang et al. (2013)	QS	SF, SG	POINT, LOC	DEBOND	LOC	40.0
Chen et al. (2014a, 2014b)	QS	DWDT, SG	POINT	DEL	N/A	52.3
Haselbach et al. (2016)	QS	DWDT, FBG, SP	POINT, LOC	DEBOND	PROP, LOC	34.0
Haselbach and Branner (2016)						
Sierra-Pérez et al. (2016)	QS	FBG, SG	POINT	DEBOND	N/A	13.5
Lee and Park (2016)	QS	N/A	N/A	DEBOND, DEL	N/A	48.3
Chen (2017)	QS	SG	POINT	BUCK	PROP	47.0
Beattie (1996)	F	AE	LOC	BUCK	IN, PROP, LOC	20.0
Taylor et al. (2012a)						9.0
Taylor et al. (2012b)	F	ACC, AE, GW, SG	POINT, LOC, GLOB	Crack	IN, PROP, LOC	
Tang et al. (2016)	F	ACC, AE	LOC, GLOB	Crack, DEL	PROP, LOC	45.7
van Leeuwen et al. (2002)	QS, F	SG	POINT	BUCK, Crack	N/A	3.4
Al-Khudairi et al. (2017)	QS, F	ACC, SG	POINT, GLOB	Crack, DEL	PROP	45.7
Poozesh et al. (2017)	QS, F	DIC	LOC	N/A	N/A	50.0
Chen (2019)	QS, F	SG	POINT	DEG	N/A	47.0
Chen et al. (2021)	QS, F	ACC, AE, DIC, SG	POINT, LOC, GLOB	Crack, DEBOND, DEL	PROP, LOC	14.3
Ulriksen et al. (2015)	OP	ACC	GLOB	Crack	IN, PROP, LOC	13.0
Tcherniak and Mølgaard (2017)						

Abbreviations: *Loading*: F, fatigue; OP, operating; QS, quasi-static; S-S, stand-still. *SHM systems*: ACC, accelerometer; AE, acoustic emission; DIC, digital image correlation; DWDT, draw-wire displacement transducer; FBG, fiber Bragg grating; GW, guided wave; LVDT, linear variable differential transformer; SG, strain gauge; SP, stereophotogrammetry. *Coverage*: LOC, point, local; GLOB, Global. *Damage types*: BUCK, buckling; DEBOND, adhesive joint debond; DEG, fatigue degradation; DEL, delamination; FF, fiber failure. *Detection*: IN, initiation; LOC, location; PROP, propagation; N/A, not available.

used a 3D DIC system consisting of two cameras on a blade to detect a delamination, which had initiated during fatigue testing, as well as a TE adhesive joint debond. The cameras were mounted on a scaffold tower next to the blade, recording images at a rate of 58 frames per second. Using the recorded images, cyclic buckling of the TE region caused by a TE adhesive joint debond was investigated. The size and location of the damage were inferred from the extracted strain distribution.

Accelerometers are commonly used to perform OMA on wind turbine blades, whereby the eigenfrequencies, damping ratios, and mode shapes of the structure can be estimated. Larsen et al. (2014) and Tcherniak and Mølgaard (2015) used OMA on a blade mounted on a test stand to investigate changes in modal parameters caused by the presence of damage in the blade. A similar study was performed by Tang et al. (2016), where no apparent changes in the first two eigenmodes were found as a consequence of a 0.2-meter damage in a 45.7-meter blade. Ulriksen et al. (2015) and Tcherniak and Mølgaard (2017) used an electromechanical hammer to actively excite a blade of an operating turbine and measured the vibration response with accelerometers. The SHM system enabled detection of a TE crack as well as propagation of the damage.

AE sensors are used to measure vibrations in the high-frequency range, typically between 100 kHz and 1 MHz. Material degradation, such as fiber or matrix cracking, will result in vibrations in the frequency range covered by AE sensors, which in this context are referred to as AE hits. Investigating, for example, changes in the number of AE hits within a specific time period or general increase in AE hit amplitude can give an indication of the initiation or propagation of damage. By use of multiple sensors, triangulation of the damage location can be performed, based on the wave speed in the structural material. Beattie (1996) used AE sensors to detect local buckling during fatigue testing, which ultimately resulted in blade failure. Tang et al. (2016) used AE sensors to detect damage propagation during fatigue testing, as well as to yield information concerning the location of the damage. Chen et al. (2021) used AE energy to detect damage initiation in a blade during fatigue testing.

GW systems commonly use piezoelectric transducers in a pitch–catch setup, where one or more sensors emit a vibration spectrum, which is picked up by one or more passive sensors. Through the use of active vibrations at high frequencies and high amplitudes, damages can be detected, if they cause changes in the frequency response of the structure within the excited frequency range. Sundaresan et al. (2002) utilized a GW system to detect local buckling failure during quasi-static testing. Taylor et al. (2012a, 2013) and Dervilis et al. (2012, 2014a, 2014b) used GW data and machine learning algorithms to detect novelties during fatigue testing of a blade, which enabled the detection of local damage.

Based on the presented literature review, there are different sensing systems available, which can be useful for blade SHM. The scope of the present work is to use a combination of the mentioned sensing systems simultaneously, such that their opportunities and limitations can be compared. On top of that, this work presents an active vibration-based SHM system, which is tested together with existing sensing systems. The sensing systems are used for detection and monitoring of different damages during fatigue testing of a 52-meter wind turbine blade. The damages investigated are laminate cracks, located in different parts of the blade. This paper focuses on one of the damage cases, being a laminate crack in the web transverse to the spanwise direction. This damage case is chosen, since progressive damage development during fatigue testing is obtained continuously after manual introduction of the crack. Based on preliminary analysis of the recorded sensor data, opportunities and limitations of the different sensing systems for use in blade SHM are investigated. The paper is structured as follows: The blade, test setup, damage cases, and sensing systems are presented in Section 2. Observations from progression of the transverse crack in the web laminate are presented in Section 3. For the same damage case, sensor data from the blade test are presented and discussed in Section 4, and conclusions on the opportunities for using the investigated sensing systems for blade SHM are drawn in Section 5.



Figure 1. A 52-meter blade on test stand at the Siemens Gamesa Blade Test Center in Aalborg, Denmark. The blade is mounted pressure side up for flapwise fatigue testing. The image shows the blade without the fatigue exciter mounted.

2. Test Setup for Blade Structural Health Monitoring

The following presents the wind turbine blade used for the fatigue test campaign, the blade test setup, the investigated damage cases, as well as the utilized sensing systems, and the FE model of the blade used for simulations.

2.1. Blade test setup

For the present test campaign, a 52-meter wind turbine blade is used. The blade was manufactured from glass fiber reinforced epoxy resin with balsa and plywood core materials. Resin infusion was performed in a single shot through the IntegralBlades technology (see Stiesdal et al., 2003). The blade is mounted pressure side (PS) up on an indoor test stand (see Figure 1). The blade test is performed at the Siemens Gamesa Blade Test Center in Aalborg, Denmark. The test hall blocks out wind and is temperature regulated, which helps in limiting the influence of variations in environmental conditions on the state of the wind turbine blade and of the SHM systems. The ambient temperature inside the hall is maintained between 25 and 26°C for the majority of the time. It is, however, not part of this study to investigate active compensation of environmental and temperature effects. Thus, environmental and temperature effects are desired to be filtered out passively, which is done by conducting the test inside the test hall.

In the presented test campaign, both flapwise and edgewise fatigue testing are conducted in sequence. Thus, two different fatigue exciters are mounted on the blade at different points in time during the test campaign. Multiple types of sensing systems are used: SGs, FBGs, a DIC system, AE sensors, accelerometers, an active vibration monitoring system, and a GW pitch-catch system. Some of the sensing systems are collecting data continuously during fatigue testing, stand-still, and flapwise hand-excitation of the blade tip, whereas others collect data periodically. An overview of fatigue test uptime, damage introductions, and repairs is shown in Figure 2. Four different damage cases are investigated over the course of the test campaign. The normalized strain range, averaged over 10-minute intervals, is plotted in Figure 2. The signal is sampled from an SG at spanwise position 34 m, placed on the PS, measuring flapwise normal strain. Some changes and fluctuations in the applied load can be observed. The applied flapwise load is increased by 10% on October 29 and by an additional 10% on December 9, 2020. Fluctuations in the applied load were caused by issues with the flapwise fatigue exciter, which were ultimately fixed.

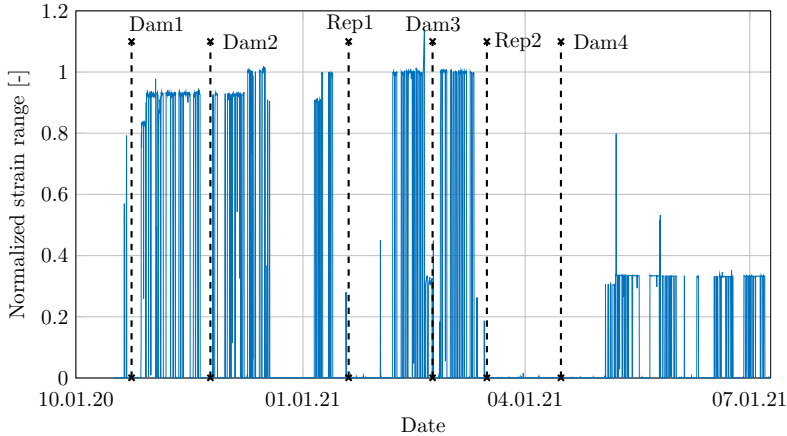


Figure 2. Flapwise normal strain range during test campaign, showing time of damage introduction (Dam1–Dam4), repair (Rep1 and Rep2), and test uptime. Testing with damage #1, damage #2, and damage #3 (Dam1, Dam2, and Dam3, respectively) is performed in flapwise fatigue, whereas testing with damage #4 (Dam4) is performed in edgewise fatigue. Due to the SG measuring flapwise normal strain, the strain range is lower during edgewise fatigue testing, compared to flapwise fatigue testing.

2.2. Damage cases

The considered damage cases are based on damages observed in literature on blade tests. Common damage types in wind turbine blades were reviewed by Sørensen et al. (2004), with the presented damage types being based on observations from quasi-static testing of a wind turbine blade. These include the following: adhesive bondline damage, sandwich face/core debonding, delamination, cracking along the fiber direction, and buckling damage. Due to the use of the IntegralBlades technology for the manufacturing of the blade used in this work, there are no bondlines between the PS and SS shells. Thus, bondline damages are not relevant for this blade.

For this work, cracks transverse to the spanwise direction, located in the blade shell and blade web, are studied. Transverse cracks may initiate from manufacturing defects such as transverse wrinkles, as investigated by Leong et al. (2012). Artificial cracks are induced in the 52-meter blade by use of a small angle grinder, cutting through the thickness of the laminate. A total of four damage cases are investigated, denominated damage #1–#4, with their global position sketched on the blade in Figure 3. Images of the damages are shown in Figure 4. Descriptions of the damage cases, their global spanwise position, and the manual lengths induced are presented in Table 2. Damage #3 is selected for analysis in this paper, since progressive damage development was obtained continuously after manual introduction of the damage.

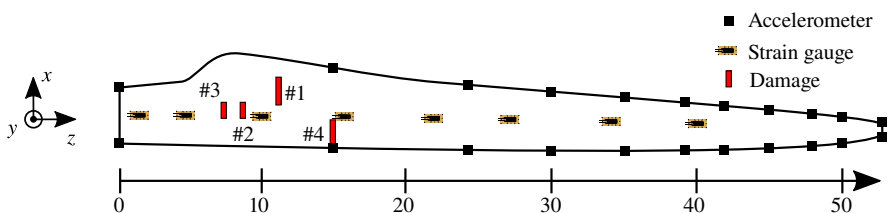


Figure 3. Spanwise and edgewise placements of investigated damage cases, including global unidirectional SG and triaxial accelerometer placement. All dimensions in meter. At positions marked with SGs, SGs are placed on the suction side, pressure side, leading edge, and trailing edge, respectively.

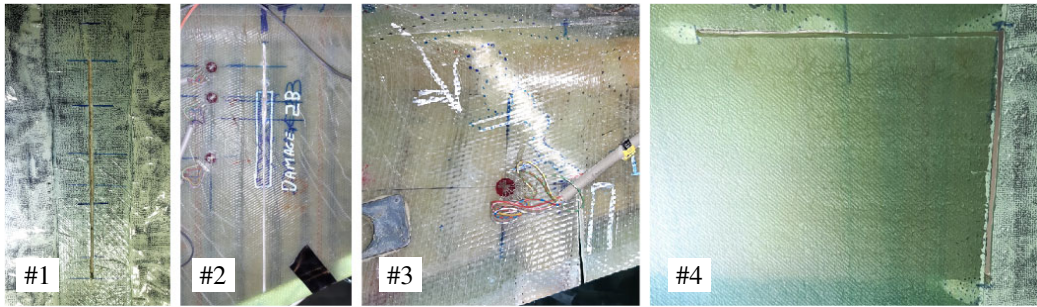


Figure 4. Investigated damage cases. #1: Transverse crack in pressure side shell. #2: Transverse crack in web start. #3: Transverse crack in web start. #4: Transverse/longitudinal crack in leading edge shell.

Table 2. Overview of the investigated damage cases.

Damage case	Description	Spanwise position [m]	Manually induced crack length [mm]
#1	Crack in PS shell, toward TE	11	70
#2	Crack in web start	7.5	30
#3	Crack in web start	6.5	100
#4	Crack in LE shell	15	200

Abbreviations: LE, leading edge; PS, pressure side; TE, trailing edge.

The damage is initiated as a transverse crack in both the PS and SS parts of the web start, as will be elaborated in Section 3.

2.3. Sensing systems

The main objective of the presented blade test is to use various sensing systems to record data for healthy and damaged states of the blade. These data can then also serve as a basis for future studies on SHM in wind turbine blades, with the purpose of investigating the opportunities and limitations of the different sensing systems for damage detection in large wind turbine blades. The used sensing systems, listed in Table 3, include pointwise sensors (such as SGs), local damage detection systems (such as AE sensors), and global damage detection systems (such as a series of distributed accelerometers combined with subsequent data analysis). Local damage detection systems are useful for detection of damages within a limited area, for example, within a radius of 1 m from each sensor in a cluster of sensors. A global damage

Table 3. Overview of the used sensing systems.

Sensing system	Number of sensors	Coverage	Distance from damages [m]
Strain sensors	64	Local and global	0.1–30
Digital image correlation	1	Local	0–0.5
Acoustic emission	4	Local	0.25–0.5
Distributed accelerometers	22	Global	1–30
Active vibration monitoring	11	Local and global	1–15
Guided waves	16	Local	0.25–0.5

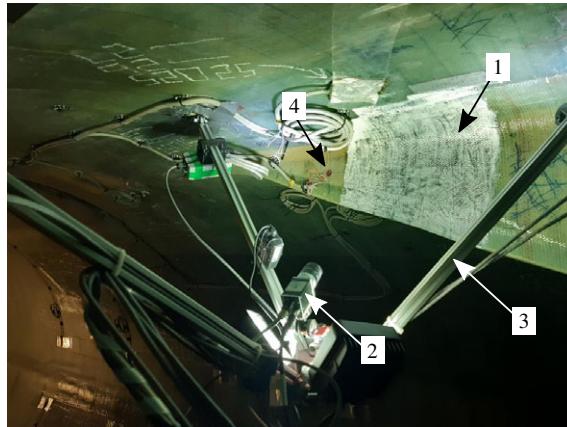


Figure 5. Sensing systems near damage #3. DIC system 1: Black-and-white speckle pattern; 2: Digital camera; 3: Tripod fixture with LED lights. 4: Strain rosette on the web start near damage #3.

detection system should, ideally, facilitate detection of damages in the entire blade. In addition, to the listed sensing systems, a digital camera was placed inside the blade to enable surveillance of the damages during testing.

2.3.1. Strain sensors

The load level in wind turbine blades during fatigue testing is commonly evaluated by use of SGs. In the present blade test, various SGs are distributed along the span of the blade. Unidirectional SGs are placed on the PS, SS, leading edge (LE), and TE at multiple spanwise positions between 1 and 40 m, as shown in Figure 3. In addition, SGs are placed locally near the positions of damage #1–#3. An SG placed near damage #3 is shown in Figure 5. For this damage, strain rosettes are used to measure in-plane strain in multiple directions near the damage. The type of unidirectional SG used is a Vishay WD-DY-375BG-350, and the type of strain rosettes used is a Tokyo Measuring Instruments Lab. FRAB-10-11. A custom measurement system in accordance with IEC 61400-23 and ISO 17025 is used.

As an addition to the SGs, FBGs are installed at multiple positions near the conventional foil gauges to measure spanwise normal strain. Thus, the performance of the two different strain sensors may be compared over the course of the fatigue testing campaign.

The local SGs are placed to monitor progression of the respective damages over time, which will have an influence on the local strain distribution. The strain magnitudes near crack tips will increase, whereas strain magnitudes near free crack faces will decrease. Thus, information about the location and size of a damage can also be inferred, if a sufficient number of strain sensors are located near a damage.

2.3.2. Digital image correlation

A DIC system, designed by the IRT Jules Verne and the University of Nantes, is used to continuously monitor the full-field strain distribution around the damages, also during fatigue testing. By mounting the DIC system on a tripod fixture inside the blade, the DIC system is subjected to the same global displacements as the blade, and local displacements of the region of interest are obtained directly. A black-and-white speckle pattern is applied to the damaged area (see Figure 5). A base layer of white paint is applied, on top of which a random speckle pattern is applied using a stamp roller from a Correlated Solutions Speckle Pattern Application Kit. A tripod fixture is used to mount a digital camera, which captures images of the painted area periodically. By having full-field strain distributions available for the

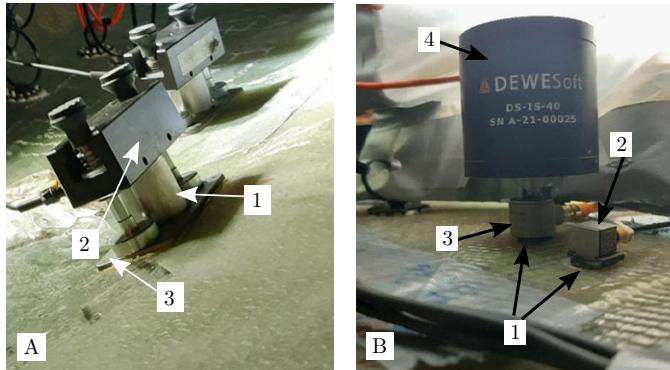


Figure 6. *A: Acoustic emission (AE) sensor setup; 1: AE sensor; 2: Magnetic clamping fixture used to fix the AE sensor to the blade; 3: Steel mounting plate adhered to the blade laminate. B: Active vibration monitoring system; 1: Mounting plates adhered to the blade laminate; 2: Accelerometer; 3: Force transducer; 4: Vibration shaker.*

damaged area, changes in the strain magnitude, caused by the damages, can be inferred. Propagation of the damages will thus be visible from the recorded images.

2.3.3. Acoustic emission

An AE system is used to continuously monitor AE activity close to the damages during fatigue testing. A Vallen AMSY-6 system with four VS900 piezoelectric AE sensors is utilized. Figure 6a shows AE sensors placed near damage #3. AE sensors measure high-frequency vibrations, with the utilized system capturing vibrations within a range between 100 and 900 kHz. Using the AE data from the test, damage propagation may be indicated by, for example, increased AE hit count or an increase in intensity of the AE hits. Damage initiation and propagation may thus be inferred directly from the recorded data. AE data are recorded continuously during the test, with all hits below 40 dB being filtered out. The filtering removes a large part of noisy scatter from the fatigue test, which would otherwise be counted as false-positive hits.

2.3.4. Distributed accelerometer system

An accelerometer-based system is used to continuously record the vibration response of the blade. Twenty-two Micron-Epsilon ACC5703 micro electromechanical systems triaxial accelerometers with a frequency range between 0 and 1,000 Hz are placed along the LE and TE of the blade, as illustrated in Figure 3. Similar accelerometer-based systems are commonly used for OMA of wind turbine blades. Using the acceleration measurements, changes in the local mechanical properties of the blade, caused by damage, may be detectable through changes in the natural vibration response of the system.

2.3.5. Active vibration monitoring system

An active vibration monitoring system, using accelerometers and an electrodynamic vibration shaker, is designed by the authors and tested in connection with the blade test. The electrodynamic shaker emits vibrations at high frequencies relative to, for example, the first 20 eigenfrequencies of the blade. The vibration response is recorded by a number of accelerometers, distributed within up to 15 m of the vibration shaker. The active vibration monitoring system consists of 11 Brüel & Kjær type 4507-B-006 piezoelectric uniaxial accelerometers with a frequency range of 0.2–6,000 Hz. The electrodynamic shaker is a DEWESoft model DS-IS-40, outputting up to 40 N between 10 and 3,000 Hz. A collocated Dytran 1053V1 force transducer is added to the mounting of the vibration shaker to allow measurement of the input force. An NI cDAQ-9185 data acquisition unit is used with three NI-9234 input modules and an

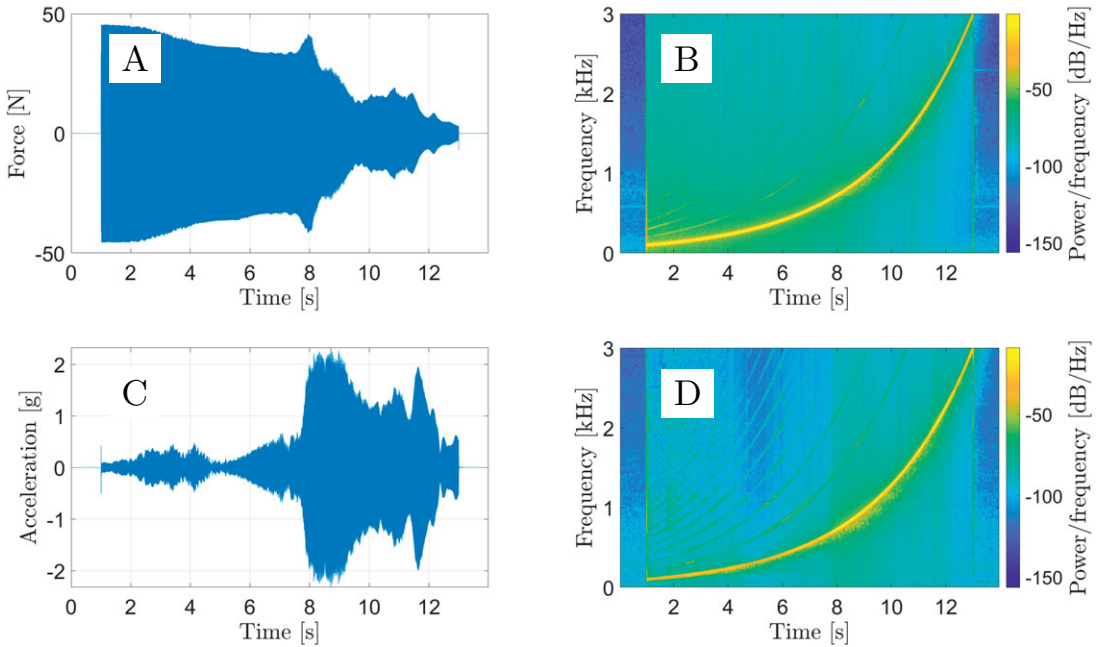


Figure 7. Chirp signal generated with electrodynamical shaker for damage #3. *A:* Time series of force input by the vibration shaker measured with a force transducer (see Figure 6b). *B:* Spectrogram of force time series in *A*. *C:* Time series of acceleration signal measured with accelerometer on the web 1 m away from shaker. *D:* Spectrogram of acceleration time series in *C*.

NI-9260 output module. Data acquisition is controlled via a laptop PC with MATLAB software. With the electrodynamical shaker, three different types of vibration signals are applied to the blade: sinusoidal burst, exponential chirp, and white Gaussian noise. The accelerometer signals are sampled at 25,600 Hz over a period of 14 s, with the active vibration input being applied 1 s after sampling begins and ended 1 s before sampling stops. See Figure 7 for an example of an applied exponential chirp signal with a frequency range of 100–3,000 Hz.

Similarly to the previously described accelerometer-based system, the active vibration monitoring system enables damage detection based on changes in the frequency response of the blade within the range of the applied active vibrations. By using an active input of vibrations with a higher frequency than, for example, the first 20 natural frequencies of the blade, the wavelengths of the vibration inputs are smaller, which means that smaller damages can be detected.

The active vibration monitoring system is similar to a system developed by Tcherniak and Mølgaard (2015), which incorporates an electromechanical hammer and a number of distributed accelerometers. The main difference between the system designed by Tcherniak and Mølgaard (2015) and the present active vibration system lies in the source of the active vibration input. Tcherniak and Mølgaard (2015) used an electromechanical actuator, which provides a high-amplitude plunger hit that excites a wide frequency range for a short time period. The present work uses an electrodynamical shaker, where the vibration frequency, amplitude, and time period of excitation can be controlled by the user through computer software.

2.3.6. Guided waves

A GW pitch–catch system, consisting of two piezoelectric actuators and two piezoelectric sensor strips with a total of 16 individual sensors, is placed around the damages to monitor the local changes caused by initiation and propagation of the damages. The GW system installed near damage #3 is shown in

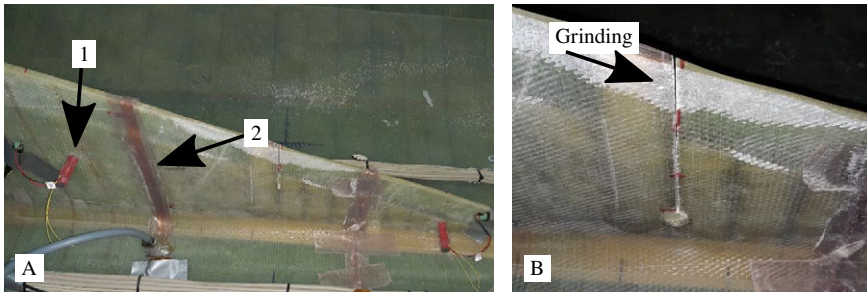


Figure 8. *A: Web start toward suction side (SS) with GW pitch–catch system installed near damage #3; 1: GW actuator; 2: GW sensor patch with eight individual sensors. B: Damage #3 on the SS part of the web start after the test was stopped with this damage case. The damage was initially introduced through grinding of the laminate on February 5, 2021. A delamination formed at the crack tip, but it propagated significantly slower than the damage on the pressure side part of the web start.*

Figure 8a. The sensor patches are placed at spanwise distances between 0.25 and 0.35 m from the investigated damages, and the actuators are placed at spanwise distances of 0.5 m from the damages. Initiation and propagation of damage can be detected through, for example, changes in amplitude and reflections of waves (see Guan et al., 2017). The GW system has been designed by the Dynamics Research Group at The University of Sheffield.

2.4. Blade finite element model

An FE model of the blade is used to perform studies on the effect of the damages on the strain distribution as well as on the modal parameters. The FE model is discretized using linear shell elements, and cracks in the laminate are modeled through nodal separation. Regarding boundary conditions, the blade is fixed at the root, and distributed loads, which correspond to the fatigue loading applied to the blade during fatigue testing, are applied to the FE model. To facilitate the use of a smaller element size around modeled damages, a submodel of the geometry in the vicinity of damages is created. At the boundary of the submodel, displacements from nodes at the same location, extracted from the global blade model, are applied. See Fremmelev et al. (2020) for further details regarding the blade FE model as well as the approach used for damage modeling. The FE model is used to estimate strain values for comparison with SG measurement. The calculated eigenfrequencies are used for comparison with eigenfrequencies estimated in the blade test through OMA, which is elaborated in Section 4.

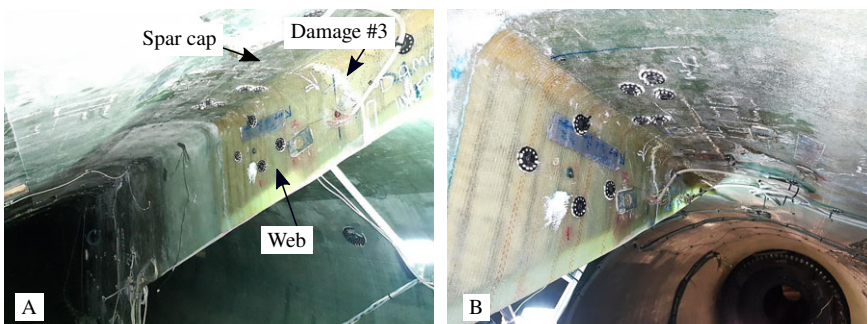


Figure 9. *Damage #3 toward the pressure side. A: Viewed toward the tip. B: Viewed toward the root.*

3. Observations from Damage Progression

This section describes how damage #3 is initiated in the blade, and what observations of the damage propagation are made. To give an overview of the geometry of the blade near the damage, Figure 9 shows the area near damage #3 toward the PS.

Damage #3 was desired to be crack in the laminate, transverse to the spanwise direction of the blade. A first attempt at initiating the damage was made by grinding down the laminate on both the LE and TE sides of the web start, which reduced the laminate thickness. This can be seen for the SS in Figure 8b, and a similar grinding was made toward the PS. The grindings resulted in a thinner laminate, which lead to larger strain magnitudes in the laminate, based on which the likelihood of damage initiation would increase. However, no visible damage initiated at the grinding in the laminate. Consequently, the damage was initiated by manually cutting through the laminate, which resulted in a crack, as shown in Figure 8b. Damage #3 was a transverse crack in the web laminate, placed close to the web start (see Figures 3 and 9). The damage was introduced in the web start toward both the PS and the SS. Starting from the web, the crack was initiated by cutting all the way through the web laminate. This resulted in the crack shown in Figures 8a and 10a, showing the web start toward the SS and the PS, respectively. Both artificial cracks had an initial length of approximately 100mm transverse to the spanwise direction. The width of the cracks corresponded to the width of the saw blade used to cut through the laminate. The crack toward the SS did not propagate significantly during fatigue testing, which is attributed to mean strains being of lower magnitude compared to those on the PS. Due to the loads induced by the self-weight of the blade, the SS and the PS are subjected to a negative and positive offset in mean load, respectively. Thus, the crack on the PS is loaded in tension–tension fatigue, which is more likely to propagate the crack than the compression–tension fatigue load on the SS. Since the crack in the PS web start propagated most, analysis of local sensor data in Section 4 is limited to the PS part of damage #3.

Figure 8a shows damage #3 on the SS part of the web start. No significant damage propagation occurred with the initial damage length of 100 mm, after which the damage length was increased to a total of 150 mm. A delamination formed at the crack tip after additional fatigue testing (see Figure 8b), but the delamination propagated significantly slower than the delamination in the PS web start. From the initial length of damage #3 toward the PS, as shown in Figure 10a, the crack propagated between approximately 45 and 60° toward the tip and the PS spar cap (see Figure 10c). Once the crack had propagated close to the spar cap, the damage propagated further as a delamination (see Figure 10c). With subsequent fatigue

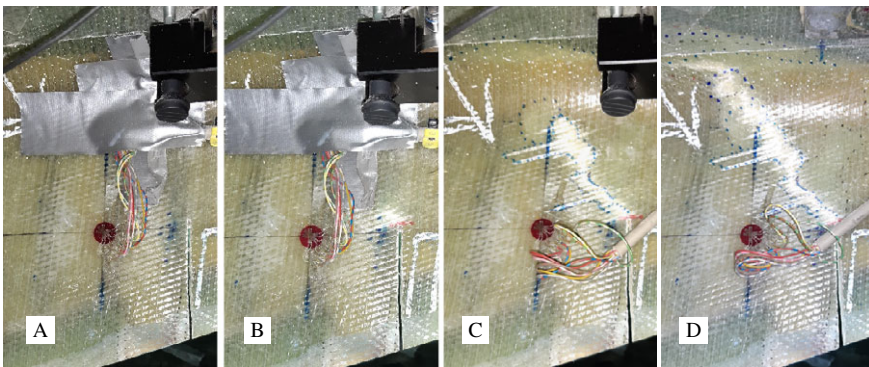


Figure 10. Damage #3 toward pressure side: Crack in web start. A: Manual introduction of transverse crack near web start (February 22, 2021). B: Delamination starts forming at the crack tip (February 26, 2021). C: Damage propagated through delamination and laminate cracking (March 22, 2021). D: Testing stopped with this damage after the delamination propagated to the spar cap and the crack reached the spar cap (March 11, 2021).

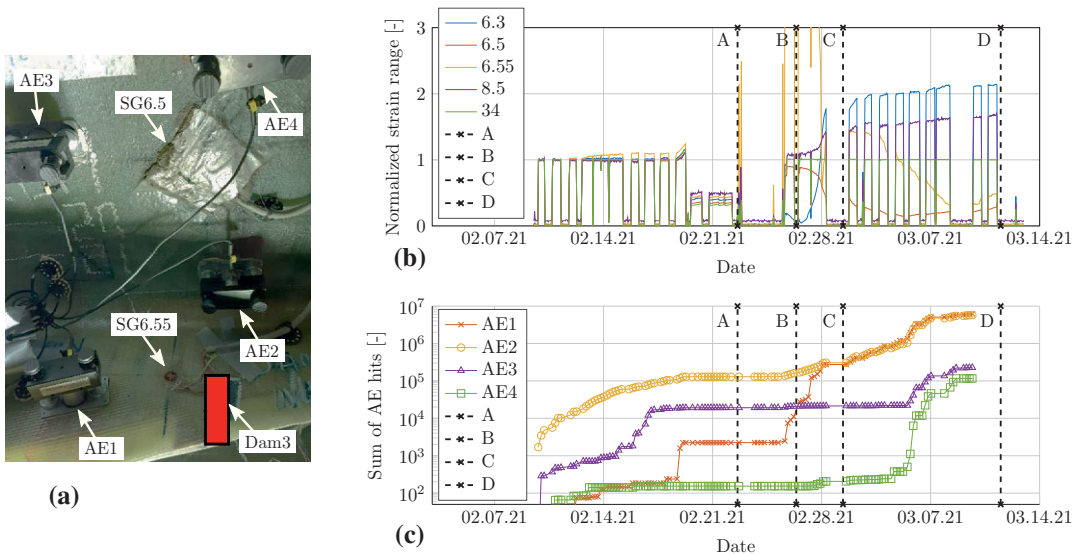


Figure 11. (a): Acoustic emission (AE) and strain gauge placement near damage #3. The location of the damage is marked with a red rectangle. (b): Normalized strain ranges $\Delta\varepsilon_{12,\text{norm}}$ (SG6.3, SG6.5, SG6.55, and SG8.5) and $\Delta\varepsilon_{11,\text{norm}}$ (SG34) for testing with damage #3. The damage was manually introduced on February 22, 2021, coinciding with the dotted line A. (c) Sum of AE hits for testing with damage #3. The four AE sensors are denominated AE1–AE4. AE measurements for the last few days of testing with this damage are not available.

testing, the damage propagated as both a crack and delamination through the spar cap (see Figure 10d). At this point, fatigue testing was stopped, and the damage was repaired.

4. Processing of Sensor Data

The following section covers processing and interpretation of sensor data recorded from SGs, AE sensors, the distributed accelerometers, and the active vibration monitoring system. Results from FE analyses are also presented and compared to the sensor data.

4.1. Strain gauge measurements

The measurements from four SGs placed near the position of damage #3 are investigated. The SGs are placed at spanwise positions 6.3, 6.5, 6.55, and 8.5 m, and are denominated SG6.3, SG6.5, SG6.55, and SG8.5, respectively, in the following. The SGs at spanwise positions 6.5 and 6.55 m are shown in Figure 11a. Figure 11b shows the normalized in-plane shear strain ranges $\Delta\varepsilon_{12,\text{norm}}$ measured by the SGs on the web laminate near damage #3, as well as the normalized in-plan normal strain range $\Delta\varepsilon_{11,\text{norm}}$ measured by an SG at spanwise position 34 m. SG6.3 is located halfway down the web start toward the PS; SG6.5 on the spar cap, 100 mm from the web; SG6.55 on the web next to the damage, halfway down the web start toward the PS; SG8.5 on the web at approximately the same height as SG6.3 and SG6.55. Measurements from SG34, placed on the PS spar cap, are included as a reference for the load level, which is steady around its nominal value during fatigue testing, thus not indicating any changes as a result of damage #3. Dotted vertical lines in Figure 11b with letters A–D refer to the images of damage #3 in Figure 10. The vertical axis in Figure 11b has been limited to 3 for better visualization of the changes apparent in SG6.3, SG6.5, and SG8.5. SG6.55 exhibits a sharp peak of approximately 6.5 times the nominal strain range, occurring on February 26, 2021, coinciding with the dotted line B. This peak drops

significantly around February 28, 2021. The normalized in-plane shear strain range $\Delta\varepsilon_{12,\text{norm}}$ for each individual SG is calculated as shown in Equation (1), and the spanwise normal strain range $\Delta\varepsilon_{11,\text{norm}}$ is calculated in the same manner using spanwise normal strain measurements.

$$\Delta\varepsilon_{12,\text{norm}} = \frac{\varepsilon_{12,\text{max}} - \varepsilon_{12,\text{min}}}{2} \frac{1}{\Delta\varepsilon_{12,\text{nom}}}, \quad (1)$$

where $\varepsilon_{12,\text{max}}$ and $\varepsilon_{12,\text{min}}$ are the maximum and minimum values of the in-plane shear strain during fatigue testing, respectively, and $\Delta\varepsilon_{12,\text{nom}}$ is the nominal shear strain range, measured in the healthy state of the blade.

As described in Section 3, damage #3 was initially introduced through grinding of the web laminate, from which a visible crack did, however, not develop during fatigue testing. The strain range of SG6.55, the yellow curve in Figure 11b, shows a slight increase in the period from February 13, 2021 to February 18, 2021, which was after introduction of the grinding, but before introduction of the laminate crack. This may indicate that some damage propagation occurred after introduction of the grinding in the web laminate. However, the damage propagation was slow and not visible during inspection. Thus, it was decided to introduce the crack manually by cutting through the laminate, which was done on February 22, 2021.

Significant changes in magnitude of all strain ranges, except for that of SG34, included in Figure 11b can be seen starting around February 27, 2021, where fatigue testing is started after manual introduction of the damage in the form of a laminate crack. SG6.55, which is placed next to the damage, shows a large increase in the strain range as a consequence of the damage being introduced. The increase in strain range is caused by the strain concentration occurring at the crack tip, which is located at approximately the same height of the web as SG6.55. The initial changes in the strain range of the other SGs in Figure 11b are minor compared to the changes from SG6.55. The large increase in strain range of SG6.55 is followed by a large drop in the strain range as the damage propagates. These changes in the magnitude of the strain range are explained by the crack tip growing past the position of the SG, and loads being redistributed around the damage. This leads to reduced strains in the laminate near the free crack faces, where SG6.55 is located. The observed changes in the strain measurements are similar to trends observed by the authors in Fremmelev et al. (2020), where numerical studies on the strain distribution near a laminate crack in a blade were studied. In the cited work, it was observed that strain magnitudes would increase as a crack grew toward the location of a strain sensor, whereas the strain magnitude would decrease once the crack tip had grown past the location of the strain sensor. This behavior was proposed to be used for the estimation of crack length and damage location.

SG6.5, which is placed on the spar cap, shows a gradual decrease in the strain range after introduction of the damage. This indicates that a reduced amount of the shear loads is transferred between the spar cap laminate and the web laminate at the spanwise position of the damage. SG6.3, which is placed on the web start, shows a large drop in the strain range after introduction of the damage. With increasing damage propagation, the strain range increases to more than twice the nominal value. For SG8.5, the strain range shows a continuous increase in magnitude after introduction of the damage and with further damage propagation. The measurement results from SG8.5 indicate that a damage in the web can be detected within a spanwise distance of at least 2 m using strain measurements.

Figure 12 shows the FE geometry of the web start, overlaying the FE results for the difference in shear strain range caused by the inclusion of damage #3 with lengths of 100 mm in both the PS and SS web starts. For reference on the geometry, see Figures 9 and 10, which show photographs of the web start. The normalized shear strain range is calculated in the same manner as for the SG measurements, shown in Equation (1). Figure 12 illustrates the distance at which the strain distribution is affected by the inclusion of damage #3. The plot shows changes in the strain distribution within a distance of approximately 0.5 m with the initial length of the manually induced damage.

Using the FE model of the blade, strain ranges at the locations of the SGs are calculated with damage lengths on the PS web between 0 mm, that is, the healthy state of the blade, and 250 mm, which corresponds to the height of the web start on the PS at spanwise location 6.5 m. The strain range results,

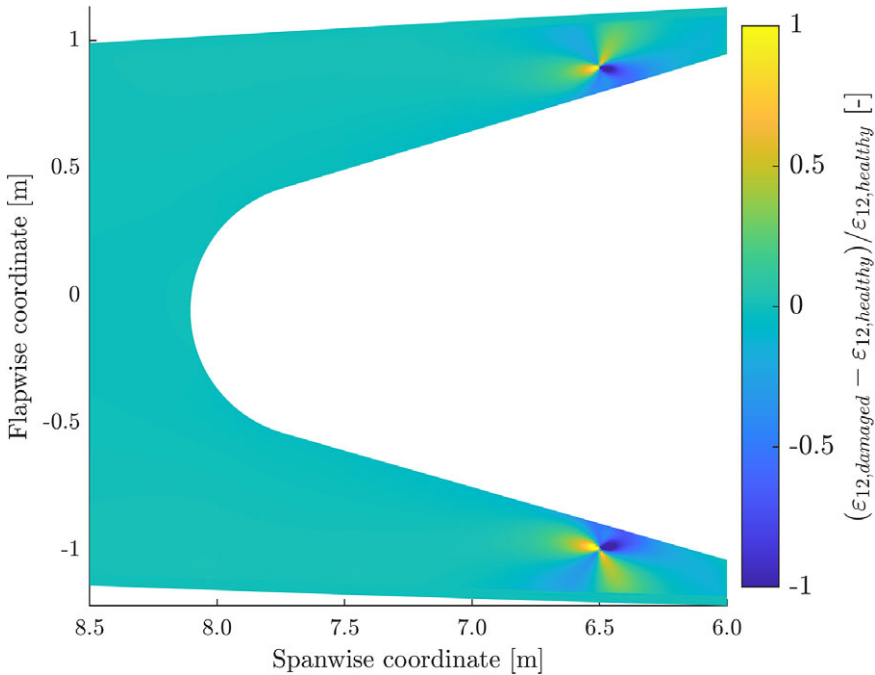


Figure 12. Difference in in-plane shear strain range at the web start between blade with the inclusion of damage #3 and the healthy blade. The damage is included at spanwise position 6.5 m with lengths of 100 mm on both the pressure side and the suction side. The color scale is limited between 1 and -1 to make changes in strain further away from the damage visible. Thus, changes in the strain range in the plot correspond to between 100 and -100% of the nominal strain range, whereas the strain range gradients of the peaks beyond this range are not readable from the plot.

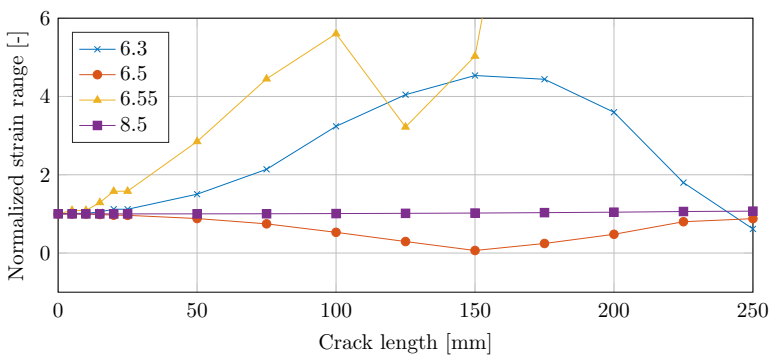


Figure 13. Normalized strain range plotted as a function of the crack length in the pressure side part of damage #3. The second axis is limited to six times the nominal strain range to cut out the peak from spanwise position 6.55 m, which is located very close to the stress concentration and will thus tend toward a nonphysically large value.

extracted at the same positions as those of the SGs presented in [Figure 11b](#), are plotted in [Figure 13](#). Only increasing damage length on the PS of the web is studied, since this is the location where the damage propagated during fatigue testing. Comparing the FE strain range in [Figure 13](#) to the SG measurements in [Figure 11b](#), the following observations are made for the four SG positions:

- **SG6.3:** The SG measurements show values of magnitudes lower than the nominal strain range after introduction of the damage with a length of 100 mm. By comparison, the FE model yields a large increase in strain range after introduction of the damage. Toward the maximum damage length, the SG measurements reach their largest value, whereas the strain range from the finite element analysis (FEA) decreases below the nominal value.
- **SG6.5:** Both SG measurements and FEA results show similar trends with a decrease in the strain range, followed by an increase in strain range.
- **SG6.55:** The large changes at SG6.55 in the FEA are due to a singularity at the crack tip, where strains approach infinity with decreasing element size. This is not physical behavior, and indicates that the measurement in the model is too close to the crack tip, and that why the magnitudes of the measurements are not accurate and comparable to SG measurements from the blade test. Considering the general trends of the FE strain range, it is very similar to the SG measurements. Both SG measurements and FEA results show a sharp increase in the strain range after introduction of the damage, followed by a slight decrease, and again followed by an increase in the strain range. For the SG measurement, a final decrease below the nominal strain range is observed (not visible in the plot due to axis limits).
- **SG8.5:** There is a large difference in the magnitude of changes in the strain range with increasing crack length. The model predicts an increase in the strain range of 7% with a damage length through the whole web height, whereas the SG measurements show an increase over 70%. The model predicted a change in the spanwise normal strain range comparable to the SG measurements of the shear strain range.

Inaccuracies of the FE model are deemed to be due to the model being relatively simple compared to, for example, a model with 3D solid elements with a fracture mechanics model for the crack. In general, although the FE model is not able to accurately approximate strain ranges for all the SGs, it is able to predict general trends in the changes occurring in some of the SG measurements due to damage initiation and progression.

4.2. Acoustic emission system

Four AE sensors are placed between 0.2 and 0.5 m from the point of damage initiation (see [Figure 11a](#)). AE data recorded during the test period for damage #3 are shown in [Figure 11c](#), with the sum of AE hits plotted along the vertical axis with logarithmic axis scaling. Damage propagation during fatigue testing is inferred from the sensor signals starting around February 27, 2021, coinciding with the dotted vertical line B, where large changes in the magnitude of the strain range are measured, and high increases in the number of AE hits are recorded. Jumps in AE hit count prior to February 27, 2021 are mainly attributed to measurement noise captured during fatigue testing. Starting February 27, 2021, jumps in AE hit count are attributed to damage propagation, for example, sensor AE4 showing a large jump just prior to March 7, 2021. At this point, the damage has grown toward the spar cap, and the sensors placed on the spar cap measure AE hits as the damage propagates further.

From the start of the fatigue test around February 10, 2021, an increase in the AE hit count is visible in [Figure 11c](#). In general, the trends from both the AE and SG measurements in [Figure 11b,c](#), respectively, indicate damage propagation, starting from the point of manual introduction of the crack. Taking the logarithmic axis scale into account, the number of AE hits occurring before manual introduction of the crack is minor, compared to subsequent increases in hit count. After introduction of the transverse crack, fatigue testing is started on February 26, 2021. From this point in time, an increase in the AE hit count can

be seen for sensor AE1, which is the AE sensor located closest to the damage and also the only AE sensor placed on the web laminate. Starting on February 27, 2021, increase in the AE hit count of sensor AE2, placed on the spar cap, is visible. This indicates that the damage has grown closer to the spar cap, where further propagation can be captured by sensor AE2. From around March 5, 2021, significant increases in AE hit counts are visible for sensors AE3 and AE4, which are also placed on the spar cap. Thus, sensors AE3 and AE4 are placed too far away from damage #3 to record the initial damage propagation. Once the damage grows to the spar cap, the AE sensors placed on the spar cap are able to detect further damage propagation. This shows that AE sensors have a limited range for detection of progressive damage growth in sandwich panels of wind turbine blades.

4.3. Distributed accelerometer system

The purpose of the distributed accelerometer system is to record data continuously and use the data for, for example, OMA of the blade. Although OMA has been chosen for the present work, other time or frequency domain methods for signal processing in the context of SHM are equally valid.

Through the use of OMA, it is not necessary to measure the excitation exerted on the structure, which substantially simplifies the measurement process. One of the basic assumptions in OMA is for the excitation to be uncorrelated white noise within the frequency range of interest. This assumption does not hold during fatigue testing, where the blade is subjected to harmonic excitation. Thus, the frequency of the harmonic excitation will be captured by the OMA algorithm, including higher-order harmonics of the excitation frequency. Similar problems would be apparent in an operating turbine, where the rotational speed of the rotor, including its higher-order harmonics, would be detected by the OMA algorithm. In such cases, it is necessary to filter out any harmonics, such that they do not pollute the results from the OMA algorithm. Considering the case of no harmonic excitation of the blade, that is, stand-still of the fatigue test, the test blade is not subjected to harmonic excitation.

Modal analysis code by Brandt (2013) and Orlovitz (2015) is used to estimate the modal parameters using a correlation-function-based stochastic subspace identification (SSI) algorithm. See Brandt (2011) for more details on the used OMA code and Van Overschee and De Moor (1996) for more details on SSI algorithms. The results from OMA are commonly visualized in a so-called stabilization diagram. Through the use of a stabilization diagram, eigenmodes of the investigated structure can be determined through visual inspection. Modes that stabilize with increasing number of poles, that is, increasing model order, have the potential for being physical modes. Computational modes, that is, nonphysical modes, will most likely also be present in a stabilization diagram, and determining the physical modes of a structure often requires prior knowledge of the structure and/or expert knowledge within the field of modal analysis.

Figure 14 shows the stabilization diagram of the blade, calculated from 10 hr of accelerometer data sampled at 25 Hz during stand-still of the fatigue test. During the course of the blade test, excitation for OMA was mainly constituted by ambient excitation inside the test hall, such as machinery, as well as footsteps inside the blade during manual inspection. A limited number of datasets with manual excitation of the blade tip is also available. Inspection of the stabilization diagram in Figure 14 shows a number of well-separated stable modes in the range between 0 and 8 Hz. At higher frequencies, modal separation is poorer, and stable physical modes are more difficult to identify. By inspecting the mode shapes corresponding to the stable poles, physical modes of the blade can be determined. By overlaying the Welch power spectral density (PSD) estimate on the stabilization diagram, physical modes can also be inferred from peaks in the PSD. The estimates of physical modes of the blade identified through OMA are listed in Table 4, together with the estimates calculated by use of the blade FE model. Eigenmodes are estimated for the blade in healthy and damaged condition, respectively, where the damage state considered is the furthest propagation of damage #3.

For these physical modes, no significant change in the eigenfrequencies is observed as a consequence of the furthest propagation of damage #3. This is to be expected, since the damages, which are relatively small in size compared to the span of the blade, are not assumed to significantly decrease the global

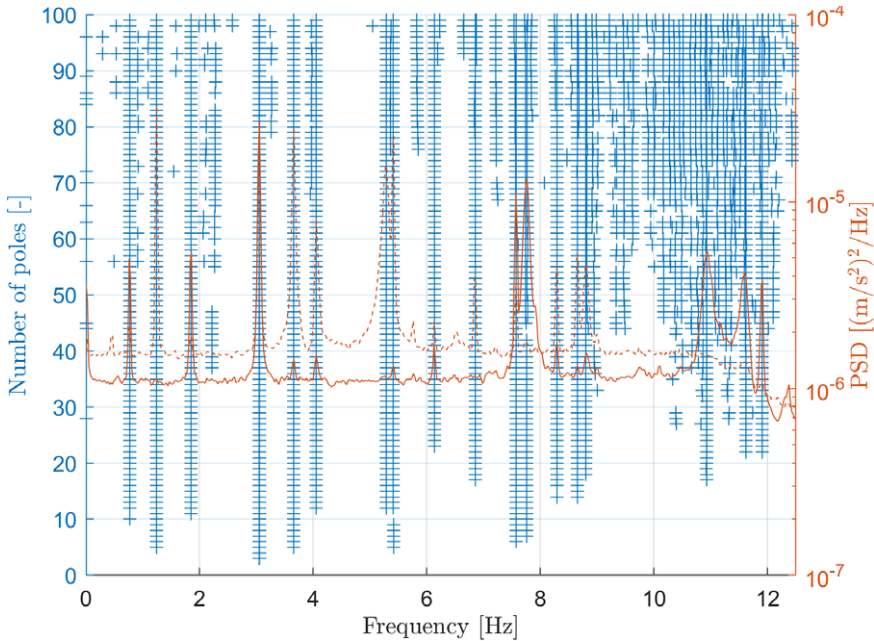


Figure 14. Stabilization diagram from 10 hr of accelerometer data, sampled while the fatigue test was not running. Due to the limited ambient excitation inside the test hall, long time series of data are necessary to enable estimation of lower-order modes of the blade. Crosses mark stable poles; unstable poles are not shown. Solid and dashed orange lines show the Welch PSD estimate of the flapwise and edgewise acceleration signals, respectively.

Table 4. List of eigenmodes calculated by OMA and FEA. The modes are calculated for the blade mounted with the flapwise fatigue exciter. N/A: not available; mode could not be identified consistently with OMA. Damaged state refers to the furthest propagation of damage #3, as shown in Figure 10d.

Mode	Description	OMA healthy [Hz]	OMA damaged [Hz]	FEA healthy [Hz]	FEA damaged [Hz]
#1	1st flapwise	0.458	0.453	0.461	0.461
#2	1st edgewise	0.766	0.764	0.759	0.759
#3	2nd flapwise	1.240	1.236	1.264	1.263
#4	2nd edgewise	3.048	3.048	2.478	2.478
#5	3rd flapwise	3.655	3.654	3.696	3.695
#6	4th flapwise	N/A	N/A	5.292	5.287
#7	1st torsional	7.755	7.755	6.834	6.834

stiffness of the blade, as shown by Larsen et al. (2014). Thus, the lower-order modes are not expected to be significantly impacted by the presence of the investigated damages. Damage of relatively small size compared to the length of the blade will thus only be detectable in higher-order modes, given the use of raw eigenfrequencies.

Using the blade FE model with and without the inclusion of a crack in the web, modal analyses are performed to estimate the eigenfrequencies of the blade. Deviations between the eigenfrequency

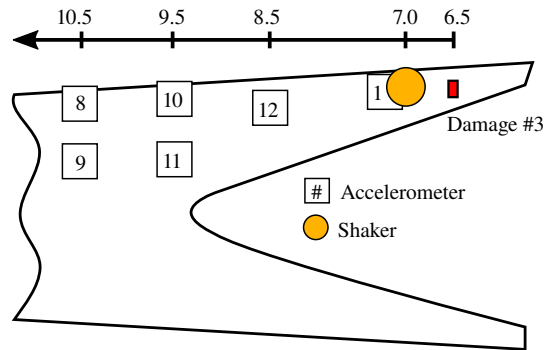


Figure 15. Accelerometer placement near damage #3. Accelerometers #2–7 are placed along the LE and TE between spanwise positions 8 and 14 m. This work investigates measurements from accelerometers #9 and #12.

estimates from OMA and FEA are attributed to measurement uncertainties, lack of excitation of individual modes, modeling inaccuracies, and uncertainties with respect to placement and weight of the fatigue exciter. The utilized FE model is not tuned for modal analysis, which is why inaccuracies in eigenfrequency estimation may be expected. The purpose of using the FE model is not to enable accurate estimation of eigenfrequencies, but instead to make possible the investigation of changes in eigenfrequencies caused by damages.

4.4. Active vibration monitoring system

Use of the presented active vibration monitoring system is investigated for blade SHM. The active vibration monitoring system, shown in Figure 6b, consists of 11 accelerometers, a force transducer, and an electrodynamic vibration shaker. Positioning of accelerometers and the vibration shaker on the web start is shown in Figure 15. The vibration signal emitted by the vibration shaker is a logarithmic chirp, with a frequency range between 100 and 3,000 Hz. The time and frequency responses of a chirp signal from both the force transducer and an accelerometer are shown in Figure 7. Using the logarithmic chirp signal as vibration input, the PSD is calculated from the sampled acceleration response. Two PSD responses for the healthy blade as well as four PSD responses with increasing severity of damage #3 are plotted in Figure 16, shown for two different accelerometers. The placement of the accelerometers relative to the vibration shaker and damage #3 is shown in Figure 14. The PSDs are calculated from acceleration time series such as the one shown in Figure 7c. Each PSD is calculated from the average of five subsequent chirp signals in order to filter out random noise. The two first PSDs are calculated based on acceleration signals from two different dates with the blade in healthy state (February 9, 2021 and February 21, 2021). Damage #3 is introduced in the web laminate on February 23, 2021. The PSDs from February 23, 2021 and subsequent PSDs are calculated from acceleration signals with increasing damage length. In general, the PSDs sampled at healthy state of the blade, at different days, show a significantly higher degree of similarity than they do with the PSDs sampled at the damaged state of the blade. With reference to Figure 16, comparing PSDs in the healthy state to PSDs in the damaged states, various differences can be observed, as explained in the following examples:

- **Peaks/valleys appearing/disappearing:** Around 2,600 Hz for accelerometer #12, a peak in the PSD is present in the healthy state of the blade. With increasing damage length, the peak disappears and turns into a valley.

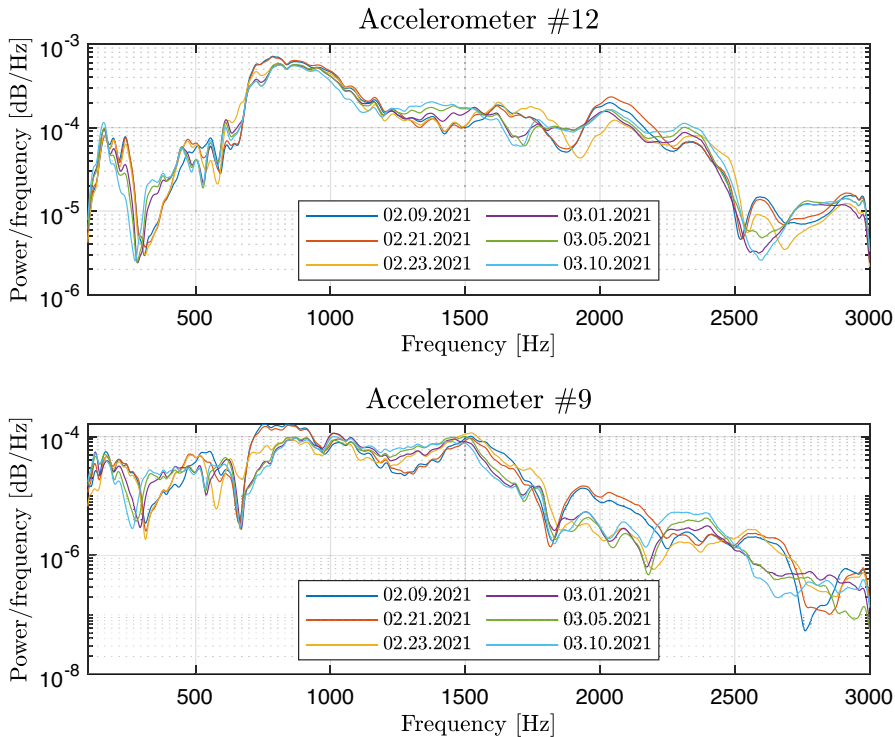


Figure 16. Power spectral densities of chirp vibration signal, sampled at healthy and damaged states of the blade. Accelerometers #12 and #9 are placed 2 and 4 m from the damage in the spanwise direction toward the tip, respectively (see Figure 15).

- **Peaks/valleys shifting frequency:** Around 300 Hz for both accelerometers, valleys in the PSD decrease in frequency with increasing damage length.
- **Peaks/valleys changing magnitude:** Between 1,900 and 2,100 Hz for accelerometer #9, peaks decrease in magnitude after introduction of the damage.

The changes in the PSD for accelerometer #12 from 2 days with healthy state of the blade (February 9, 2021 and February 10, 2021), as well as the changes in PSD from the healthy to the most severely damaged state of the blade (February 9, 2021 and March 10, 2021) are highlighted in Figure 17. Changes in PSD from, for example, February 9, 2021 to February 21, 2021 are very similar to the changes observed from February 9, 2021 to February 10, 2021.

Changes in the PSDs are deemed to be due to changes in the local vibration response of the blade as a consequence of initiation and progression of the damage. The change in local vibration response results in changes to the local modal parameters, which result in changes to the PSDs. As can be seen from the PSDs of the measurements from the two different accelerometers in Figure 16, the local structural response at the position of the accelerometer has a large influence on the frequencies and magnitudes of peaks in the PSDs. Thus, PSDs of the vibration measurements from accelerometers at different positions will have different magnitude distributions. As such, changes in the PSDs of vibration measurements from each individual accelerometer should be tracked over time and used as an indication for the initiation and propagation of damage.

Due to the test hall being a temperature-controlled environment, temperature effects can be ruled out as a cause for changes in the PSDs. Other possible causes for changes in the PSDs include, for example,

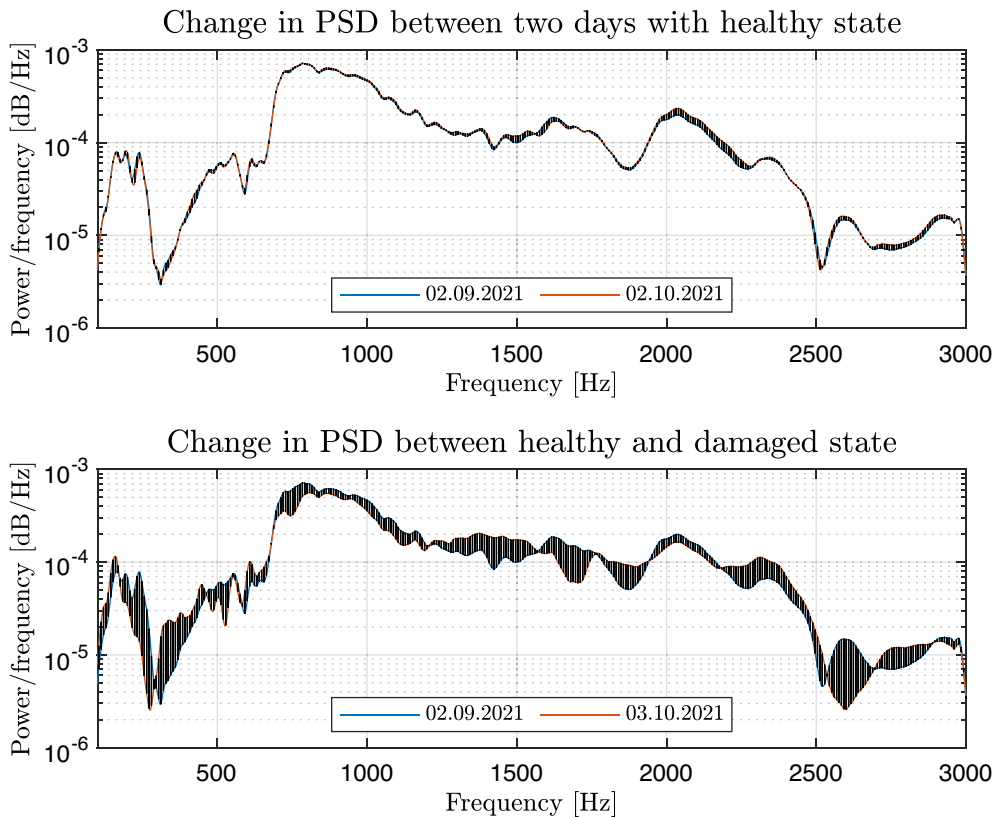


Figure 17. Change in power spectral density using accelerometer #12 between 2 days with healthy state as well as healthy and most severely damaged state. Shading with black lines highlights the change in magnitude.

changes in boundary conditions between the active vibration shaker and the blade. This could be due to relaxation of the adhesive used to mount the shaker, or the shaker breaking off the blade laminate. Experiments with the latter were performed, where it was found that breaking off the shaker and remounting it at a distance of 50 mm from the original position produced insignificant changes to the PSDs compared to those observed over the course of testing with damage #3. The observed changes in the PSD were comparable to the differences in the PSDs for the healthy blade shown in Figure 16, except for accelerometer #1, which was placed right next to the vibration shaker.

5. Conclusions

This work investigated SHM of a 52-meter wind turbine blade during fatigue testing. Multiple artificial damages were introduced in the blade laminate, and damage propagation during fatigue testing was studied. Focus was put on one of the damage cases, denominated damage #3, being a crack transverse to the spanwise direction of the blade, located in the laminate of the web start. Different sensing systems were used to record data during testing, with this work focusing on the following: SGs, AE sensors, a distributed accelerometer system, and an active vibration monitoring system. Data from the sensing systems were processed, and the capabilities and limitations of the sensing systems for use in blade SHM were investigated.

Regarding initiation and propagation of artificial damages, damages were initiated by straight through-thickness cuts in the blade laminate. Damage #3 propagated progressively during fatigue testing. Overall, having achieved fatigue-driven damage propagation through the height of the web start on the PS, including delamination growth through the web and toward the spar cap, was viewed as a success. Data from the utilized sensing systems are thus available for progressively increasing damage severity. These data can be used for more detailed investigations concerning blade SHM. Results from the DIC system and the GW system have not been presented in this work, but are of interest for future studies.

Considering the sensor data investigated in this work, the results from multiple sensing systems can be interpreted to show damage propagation. The following conclusions are drawn for the respective sensing systems:

- **SG measurements:** Damage initiation and propagation was detectable locally through the strain range. This required limited data processing, and damage initiation as well as propagation could be interpreted through changes in the magnitude of the strain range, with load-controlled fatigue that did not vary significantly. The observations from damage #3 indicated that damages in the web can be detected within a distance of at least 2 m, using SGs placed on the web or on the spar cap. Thus, SGs may be useful for local SHM of critical areas.
- **AE system:** An increase in the number of AE hits measured by the AE sensors were interpreted as the damage propagating near the sensors. By having multiple sensors placed near the damage, the location of the damage and its direction of propagation could be inferred. The area covered by AE sensors is relatively small, compared to other sensors, due to the high attenuation of high-frequency vibrations in the laminate. Based on the findings in this work, damages in wind turbine blades are estimated to be detectable within a distance of approximately 0.5 m in sandwich panels such as the web and the shell by use of AE sensors.
- **Distributed accelerometer system:** It was shown that OMA could be performed with the available data, where the blade had been subjected to limited ambient excitation, as well as no manual excitation with, for example, modal hammers. The lower-order modes could be identified with limited excitation of the blade, whereas modes above approximately 8 Hz had poor separation. Initiation and propagation of damage could not be detected by use of the raw eigenfrequency values estimated through OMA. Subjecting the blade to more ambient excitation, such as wind and rain, it is believed that modal separation will improve, enabling identification of a larger number of modes. Having more modes available may prove useful in use for blade SHM. Future work with this sensing system may include formulation of a damage index based on multiple modes, taking into account eigenfrequencies as well as mode shapes and modal damping estimates.
- **Active vibration monitoring system:** The local vibration response of the blade, caused by an active vibration input, was measured using distributed accelerometers. Using the recorded acceleration data, the PSDs were shown to change with increasing damage progression. The active vibration monitoring system proved to be more sensitive to small damages than the distributed accelerometer system, which relied on ambient excitation of the blade. Based on PSDs of the acceleration data, formulation of a damage index based on, for example, peak location and magnitude, may be used to quantify the damage severity and thus to indicate damage progression. Damage is expected to be detectable within the range of coverage of the used accelerometers, which is up to 7.5 m in the case of damage #3, based on findings in the previously cited work on a similar active vibration system. Furthermore, since multiple accelerometers were distributed along the blade span, it may also be possible to infer the location of the investigated damages from the recorded data.

Through the presented results, it has been shown that multiple sensing systems show promise for use in blade SHM. SGs and AE sensors can be used for local damage detection in critical areas. For global blade SHM, vibration-based methods have shown promise, and further studies on these methods should thus be conducted.

Acknowledgments. The DIC system was designed by Axel Guiroy, IRT Jules Verne, and Marc Francois, University of Nantes, who also conducted analysis of data collected with the system. The GW system was designed by Marcus Haywood-Alexander and Nikolaos Dervilis, The University of Sheffield. Finally, the help of the engineers and technicians at the Siemens Gamesa Blade Test Center in Aalborg, Denmark, throughout the entire test campaign is greatly appreciated.

Data Availability Statement. With the use of multiple sensing systems and a test campaign lasting over half a year, a wealth of data from the blade test is available. Interested readers are welcome to contact the authors regarding opportunities for future collaborations on data processing for SHM of blades.

Author Contributions. Conceptualization: all authors; Methodology: all authors; Data curation: M.A.F., P.L., and E.O.; Data visualization: M.A.F., P.L., and E.O.; Writing—original draft: M.A.F.

Funding Statement. This work received partial funding from the Innovation Fund Denmark, grant no. 9065-00200B. This work is partly supported by the Danish Energy Agency through the Energy Technology Development and Demonstration Program (EUDP), grant no. 64018-0068. The supported project is RELIABLADE: Improving Blade Reliability through Application of Digital Twins over Entire Life Cycle.

Competing Interests. The following guest editors were partners in the presented blade test: Nikolaos Dervilis and Keith Worden.

References

- Al-Khudairi O, Hadavinia H, Little C, Gillmore G, Greaves P and Dyer K** (2017) Full-scale fatigue testing of a wind turbine blade in flapwise direction and examining the effect of crack propagation on the blade performance. *Materials (Basel)* 10(10), 1152.
- Beattie A** (1996) Acoustic emission monitoring of a wind turbine blade during a fatigue test. *Technical Report*, Sandia National Laboratories.
- Brandt A** (2011) ABRAVIBE: A MATLAB toolbox for noise and vibration analysis and teaching. Available at <http://www.abravibe.com>.
- Brandt A** (2013) The ABRAVIBE toolbox for teaching vibration analysis and structural dynamics. In Allemang, R., De Clerck, J., Niezrecki, C., Wicks, A. (eds) Special Topics in Structural Dynamics, Volume 6. *Conference Proceedings of the Society for Experimental Mechanics Series*, pp. 131–141, Springer, New York, NY.
- Chen X** (2017) Experimental investigation on structural collapse of a large composite wind turbine blade under combined bending and torsion. *Composite Structures* 160, 435–445.
- Chen X** (2019) Experimental observation of fatigue degradation in a composite wind turbine blade. *Composite Structures* 212, 547–551.
- Chen X, Berring P, Madsen S, Branner K and Semenov S** (2019) Understanding progressive failure mechanisms of a wind turbine blade trailing edge section through subcomponent tests and nonlinear FE analysis. *Composite Structures* 214, 422–438.
- Chen X, Semenov S, McGugan M, Hjelm Madsen S, Cem Yeniceli S, Berring P and Branner K** (2021) Fatigue testing of a 14.3 m composite blade embedded with artificial defects—Damage growth and structural health monitoring. *Composites Part A: Applied Science and Manufacturing* 140, 106189.
- Chen X, Zhao W, Zhao X and Xu J** (2014a) Failure test and finite element simulation of a large wind turbine composite blade under static loading. *Energies* 7(4), 2274–2297.
- Chen X, Zhao W, Zhao X and Xu J** (2014b) Preliminary failure investigation of a 52.3 m glass/epoxy composite wind turbine blade. *Engineering Failure Analysis* 44, 345–350.
- Dao C, Kazemtabrizi B and Crabtree C** (2019) Wind turbine reliability data review and impacts on levelised cost of energy. *Wind Energy* 22(12), 1848–1871.
- Dervilis N, Choi M, Antoniadou I, Farinholt K, Taylor S, Barthorpe R, Park G, Farrar C and Worden K** (2014a) Machine learning applications for a wind turbine blade under continuous fatigue loading. *Key Engineering Materials* 588, 166–174.
- Dervilis N, Choi M, Antoniadou I, Farinholt K, Taylor S, Barthorpe R, Park G, Worden K and Farrar C** (2012) Novelty detection applied to vibration data from a CX-100 wind turbine blade under fatigue loading. *Journal of Physics Conference Series* 382(1), 012047.
- Dervilis N, Choi M, Taylor S, Barthorpe R, Park G, Farrar C and Worden K** (2014b) On damage diagnosis for a wind turbine blade using pattern recognition. *Journal of Sound and Vibration* 333(6), 1833–1850.
- Fremmelev M, Ladpli P, Bernhammer L, McGugan M and Branner K** (2020) Numerical study on the use of strains for detection of damage in wind turbine blades. *16th EAWE PhD Seminar on Wind Energy*.
- Guan R, Lu Y, Duan W and Wang X** (2017) Guided waves for damage identification in pipeline structures: A review. *Structural Control and Health Monitoring* 24(11), 1–17.
- Haselbach P and Branner K** (2016) Initiation of trailing edge failure in full-scale wind turbine blade test. *Engineering Fracture Mechanics* 162, 136–154.
- Haselbach P, Eder M and Belloni F** (2016) A comprehensive investigation of trailing edge damage in a wind turbine rotor blade. *Wind Energy* 19(10), 1871–1888.

- Jensen F, Falzon B, Ankersen J and Stang H** (2006) Structural testing and numerical simulation of a 34 m composite wind turbine blade. *Composite Structures* 76(1–2), 52–61.
- Jørgensen E, Borum K, McGugan M, Thomsen C, Jensen F, Debel C and Sørensen B** (2004) Full scale testing of wind turbine blade to failure-flapwise loading. *Technical Report*, Risø National Laboratory, Roskilde, Denmark.
- Larsen G, Berring P, Tcherniak D, Nielsen P and Branner K** (2014). Effect of a damage to modal parameters of a wind turbine blade. EWSHM - 7th European Workshop on Structural Health Monitoring, IFFSTTAR, Inria, Université de Nantes, Jul 2014, Nantes, France.
- LeBlanc B, Niezrecki C, Avitabile P, Chen J, Sherwood J and Hughes S** (2011) Full-field inspection of a wind turbine blade using three-dimensional digital image correlation. In *Industrial and Commercial Applications of Smart Structures Technologies 2011*, Vol. 7979, p. 79790L.
- Lee H and Park J** (2016) Static test until structural collapse after fatigue testing of a full-scale wind turbine blade. *Composite Structures* 136, 251–257.
- Leong M, Overgaard LC, Thomsen OT, Lund E and Daniel IM** (2012) Investigation of failure mechanisms in GFRP sandwich structures with face sheet wrinkle defects used for wind turbine blades. *Composite Structures* 94(2), 768–778.
- Orlowitz E** (2015) *Damping Estimation in Operational Modal Analysis*. PhD thesis, University of Southern Denmark.
- Overgaard L and Lund E** (2010) Structural collapse of a wind turbine blade. Part B: Progressive interlaminar failure models. *Composites Part A: Applied Science and Manufacturing* 41(2), 271–283.
- Overgaard L, Lund E and Thomsen O** (2010) Structural collapse of a wind turbine blade. Part A: Static test and equivalent single layered models. *Composites Part A: Applied Science and Manufacturing* 41(2), 257–270.
- Paquette J, Van Dam J, Hughes S and Johnson J** (2008). Fatigue testing of 9 m carbon fiber wind turbine research blades. In *46th AIAA Aerospace Sciences Meeting and Exhibit*.
- Poozesh P, Baqersad J, Niezrecki C, Avitabile P, Harvey E and Yarala R** (2017) Large-area photogrammetry based testing of wind turbine blades. *Mechanical Systems and Signal Processing* 86, 98–115.
- Rumsey M, Paquette J, White J, Werlink R, Beattie A, Pitchford C and van Dam J** (2008) Experimental results of structural health monitoring of wind turbine blades. In *46th AIAA Aerospace Sciences Meeting and Exhibit*.
- Sierra-Pérez J, Torres-Arredondo M and Güemes A** (2016) Damage and nonlinearities detection in wind turbine blades based on strain field pattern recognition. FBGs, OBR and strain gauges comparison. *Composite Structures* 135, 156–166.
- Sørensen B, Jørgensen E, Debel CP, Jensen F, Jensen H, Jacobsen T and Halling K** (2004) Improved design of large wind turbine blade of fibre composites based on studies of scale effects (phase 1)—Summary report. *Technical Report*, Risø National Laboratory, Roskilde, Denmark.
- Stiesdal H, Enevoldsen P, Johansen K, Kristensen J, Nørtem M and Winther-Jensen M** (2003) Method for manufacturing windmill blades. EU Patent: 1 310 351 A1, 14 May 2003.
- Sundaresan M, Schulz M and Ghoshal A** (2002) Structural health monitoring static test of a wind turbine blade. *Technical Report March*, National Renewable Energy Laboratory, Golden, CO, USA.
- Tang J, Soua S, Mares C and Gan T-H** (2016) An experimental study of acoustic emission methodology for in service condition monitoring of wind turbine blades. *Renewable Energy* 99, 170–179.
- Taylor S, Jeong H, Jang J, Park G, Farinholt K, Todd M and Ammerman C** (2012a). Full-scale fatigue tests of CX-100 wind turbine blades. Part I: Testing. In *Industrial and Commercial Applications of Smart Structures Technologies 2012*, Vol. 8343, p. 83430Q.
- Taylor S, Jeong H, Jang J, Park G, Farinholt K, Todd M and Ammerman C** (2012b) Full-scale fatigue tests of CX-100 wind turbine blades. Part II: analysis. In *Industrial and Commercial Applications of Smart Structures Technologies*, Vol. 8343, p. 83430Q.
- Taylor S, Park G, Farinholt K and Todd M** (2013) Fatigue crack detection performance comparison in a composite wind turbine rotor blade. *Structural Health Monitoring* 12(3), 252–262.
- Tcherniak D and Mølgaard L** (2015) Vibration-based SHM system Application to wind turbine blades. *Journal of Physics: Conference Series* 628(1), 012072.
- Tcherniak D and Mølgaard L** (2017) Active vibration-based structural health monitoring system for wind turbine blade: Demonstration on an operating Vestas V27 wind turbine. *Structural Health Monitoring* 16(5), 536–550.
- Ulriksen M, Tcherniak D and Damkilde L** (2015) Damage detection in an operating Vestas V27 wind turbine blade by use of outlier analysis. In *Proceedings of the 2015 IEEE Workshop on Environmental, Energy, and Structural Monitoring Systems (EESMS 2015)*. IEEE, pp. 50–55.
- van Leeuwen H, van Delft D, Heijdra J, Braam H, Jørgensen E, Lekou D and Vionis P** (2002) Comparing fatigue strength from full scale blade tests with coupon-based predictions. *Journal of Solar Energy Engineering* 124(4), 404–411.
- Van Overschee P and De Moor B** (1996) *Subspace Identification for Linear Systems*. Kluwer Academic Publishers Group, Dordrecht, Netherlands.
- Yang J, Peng C, Xiao J, Zeng J, Xing S, Jin J and Deng H** (2013) Structural investigation of composite wind turbine blade considering structural collapse in full-scale static tests. *Composite Structures* 97, 15–29.